Petroleum Science 21 (2024) 3189–3201

Contents lists available at ScienceDirect

Petroleum Science

journal homepage: www.keaipublishing.com/en/journals/petroleum-science

Original Paper

A new method for fluid identification and saturation calculation of low contrast tight sandstone reservoir

Shuai Wang, Ran-Hong Xie *, Guo-Wen Jin **, Jiang-Feng Guo, Li-Zhi Xiao

State Key Laboratory of Petroleum Resources and Engineering, China University of Petroleum (Beijing), Beijing, 102249, China

ARTICLE INFO

Article history:
Received 11 October 2023
Received in revised form
23 March 2024
Accepted 2 July 2024
Available online 2 July 2024

Edited by Meng-Jiao Zhou

Keywords:
Low contrast reservoirs
Fluid identification
Saturation calculation
Water spectrum method
Conventional logging

ABSTRACT

The resistivity difference between oil and gas layers and the water layers in low contrast tight sandstone reservoirs is subtle. Fluid identification and saturation calculation based on conventional logging methods are facing challenges in such reservoirs. In this paper, a new method is proposed for fluid identification and saturation calculation in low contrast tight sandstone reservoirs. First, a model for calculating apparent formation water resistivity is constructed, which takes into account the influence of shale on the resistivity calculation and avoids apparent formation water resistivity abnormal values. Based on the distribution of the apparent formation water resistivity obtained by the new model, the water spectrum is determined for fluid identification in low contrast tight sandstone reservoirs. Following this, according to the average, standard deviation, and endpoints of the water spectrum, a new four-parameter model for calculating reservoir oil and gas saturation is built. The methods proposed in this paper are applied to the low contrast tight sandstone reservoirs in the Q4 formation of the X53 block and X70 block in the south of Songliao Basin, China. The results show that the water spectrum method can effectively distinguish oil-water layers and water layers in the study area. The standard deviation of the water spectrum in the oil-water layer is generally greater than that in the water layer. The new four-parameter model yields more accurate oil and gas saturation. These findings verify the effectiveness of the proposed methods.

© 2024 The Authors. Publishing services by Elsevier B.V. on behalf of KeAi Communications Co. Ltd. This is an open access article under the CC BY-NC-ND license (http://creativecommons.org/licenses/by-nc-nd/4.0/).

1. Introduction

Low contrast reservoirs refer to oil and gas reservoirs with a low ratio of resistivity to water layers (Akkurt et al., 2008). The genetic mechanism of low contrast reservoirs is complex. The additional conductivity of clay, high formation water salinity, and other factors may reduce the resistivity of the reservoirs (Belevich and Bal, 2017; Shah et al., 2019). Thus, fluid identification and saturation calculation of these reservoirs are difficult.

Two methods are commonly employed for reservoir fluid identification with conventional logging, namely the chart and curve overlap methods (Simpson and Menke, 2010). Several classic charts, such as the Pickett and Hingle charts, are still widely used by scholars (Hingle, 1959; Pickett, 1966). In addition, numerous studies have adopted specially-made charts to identify fluid under particular circumstances in different research areas (Hamada et al., 2001; Abudeif et al., 2016; Das and Chatterjee, 2018). However, both methods are associated with limitations. The chart method can only use data from one or a few points of the logging curves, and is thus easily affected by the artificial reading errors. In contrast, the curve overlap method can use the data of the entire logging curves, yet only the original information of the logging curves can be used, while the reservoir parameters obtained based on the logging curves cannot be used. Several new logging methods have recently enhanced fluid identification. Among them is nuclear magnetic resonance (NMR) logging, with the most common one-dimensional NMR methods including the differential spectrum, shift spectrum, and time domain analysis (TDA) methods (Akkurt et al., 1995, 1997; Prammer et al., 1995). Moreover, the longitudinal relaxation time–transverse relaxation time (T_1–T_2) map and transverse relaxation time–diffusion coefficient (T_2–D) map are common two-dimensional NMR methods used to identify fluid (Toumelin et al., 2004; Heaton et al., 2007). However, NMR logging is

* Corresponding author.
** Corresponding author.
E-mail addresses: xieranhong@cup.edu.cn (R.-H. Xie), jinguowen@cup.edu.cn (G.-W. Jin).

https://doi.org/10.1016/j.petsci.2024.07.005
1995-8226/© 2024 The Authors. Publishing services by Elsevier B.V. on behalf of KeAi Communications Co. Ltd. This is an open access article under the CC BY-NC-ND license (http://creativecommons.org/licenses/by-nc-nd/4.0/).

expensive and the logging time is long, limiting the application of this method. Artificial intelligence algorithms such as neural networks and support vector machines are also employed to identify reservoir fluid, yet such data-driven methods require a large amount of data as support (Liu et al., 2017; He et al., 2020).

The oil and gas saturation calculation is an important task in reservoir evaluation. Archie (1942) proposed a saturation evaluation model suitable for sandstone reservoirs. Following this, given the additional conductivity phenomenon of clay in shaly sand reservoirs (Waxman and Thomas, 1974), scholars proposed numerous other models for the oil and gas saturation calculation models, such as the Simandoux, Waxman-Smits, Indonesia, and double water models (Simandoux, 1963; Waxman and Smits, 1968; Poupon and Leveaux, 1971; Clavier et al., 1984). The Waxman-Smits model assumes that the conductivity of shaly sandstone is the result of the parallel conduction of formation water and clay cation exchange. The double water model assumes that the conductivity of shaly sandstone originates from the parallel conduction of clay water and free water. Compared with the Waxman-Smits model, the double water model considers the effect of water film on the conductivity of rocks (Clavier et al., 1984). The cation-exchange capacity (Q_v) in the Waxman-Smits and double water models is determined by core experimental, limiting the use of these two models. The Simandoux and Indonesia models use shale content and shale resistivity to characterize the additional conductivity of clay, and all model parameters can be obtained from logging curves. The effective medium model is also employed to calculate the reservoir saturation, yet it is complex and the parameters are numerous (Koelman and De Kuijper, 1997). Pore types and formation anisotropy must be considered in the application of saturation models based on resistivity (Zhu et al., 2022; Qin et al., 2023). New logging methods, such as NMR logging, array acoustic logging, and dielectric logging, also assist in the evaluation of saturation (Jain et al., 2013; Tathed et al., 2018; Shi et al., 2019; Newgord et al., 2020). NMR logging is commonly combined with resistivity logging for oil and gas saturation calculations (Coates et al., 1994). This method requires the resistivity of formation water, which is difficult to accurately obtain in areas where formation water resistivity varies greatly.

Most of wells, particularly old wells, lack the new aforementioned logging methods. Therefore, the development of fluid identification and oil and gas saturation calculation methods for low contrast tight sandstone reservoirs based on conventional logging methods is critical to the exploration and development of such hidden reservoirs. The water spectrum approach, a fluid identification method based on conventional logging methods, identifies fluid based on the distribution characteristics of apparent formation water resistivity (Fan et al., 2019). This method is convenient and intuitive, which can fully utilize the data of the entire logging curve and effectively avoids errors from artificial reading. Moreover, it can merge multiple oil-test layers into one layer to calculate a single water spectrum, avoiding the challenges caused by multi-layer joint tests. However, previous research ignores the influence of high shale content on the calculation of apparent formation water resistivity in shaly sand reservoirs. In addition, the water spectrum method is limited to qualitative reservoir fluid identification, and does not apply to the quantitative evaluation of reservoir oil and gas saturation.

In this paper, the problem of abnormal values in the calculation of apparent formation water resistivity in the Indonesia model is reported for the first time, and the influencing factors are analyzed. A new apparent formation water resistivity calculation model suitable for shaly sandstone is proposed. Based on the distribution characteristics of apparent formation water resistivity, the water spectrum is constructed for fluid identification. A new four-parameter model is then built to calculate reservoir oil and gas saturation based on the average, standard deviation, and endpoints of the water spectrum. The significance of this research is twofold. First, the introduction of a compensation term prevents the occurrence of abnormal values during the calculation of apparent formation water resistivity. Second, the calculation of oil and gas saturation is performed on a "layer" basis, effectively reducing error accumulation and improving the accuracy of the calculation results. The methods proposed in this paper are applied to the X53 and X70 blocks in the southern Songliao Basin, China, and their effectiveness is verified.

2. Geological settings

The X53 and X70 blocks of the JL Oilfield, located in the central depression area of southern Songliao Basin, China, are selected as the study blocks for this paper. In the study area, the following strata can be observed from the bottom up: basement strata, upper Jurassic strata, Cretaceous strata, Neogene strata, and Quaternary strata. The target layer Q4 formation belongs to Cretaceous strata with a general depth of approximately 2000 m. The sedimentary type of the Q4 formation is delta plain subfacies, gradually transitioning to delta front subfacies.

Table 1 reports the number of core samples and experimental methods of the target layer in the study area. The lithology is mainly mudstone, siltstone, and muddy siltstone, while the mineral components are mostly quartz, plagioclase, and clay minerals (Fig. 1). The porosity generally ranges from 5% to 10%, with a permeability range of 0.01–1 mD (Fig. 2). This indicates that the target layer belongs to a tight sandstone reservoir.

The study area contains numerous low contrast reservoirs. As well as the high bound water content and low oil and gas saturation caused by poor physical properties, the additional conductivity of clay and the variation in salinity of formation water are also sources of low contrast reservoirs in this area. The clay content is high comparatively. Illite-smectite mixed layers dominate the clay mineral components, with a strong cation exchange capacity, providing additional conductivity for the reservoirs. The average clay contents of the X53 and X70 blocks are 13.04% and 11.20%, and the illite-smectite mixed layers account for 55.60% and 70.56% of the total clay content, respectively (Fig. 3). The distribution range of formation water salinity in this region is broad (Fig. 4). The salinity of the formation water determines the resistivity of the formation water. Formation water with low resistivity will reduce the resistivity of the oil and gas layer, while formation water with high resistivity will increase the resistivity of the water layer (Bai et al., 2019). This narrows the gap in resistivity between the oil and gas

Table 1
Number of samples and experimental methods in the study area.

Block	Project	Number	Method
X53	Lithology	222	Cutting description
	Mineral components	189	X-ray diffraction
	Porosity	489	Gas measurement
	Permeability	452	Gas measurement
	Clay contents	189	X-ray diffraction
	Clay mineral components	146	X-ray diffraction
	Formation water salinity	16	Water analysis
X70	Lithology	707	Cutting description
	Mineral components	61	X-ray diffraction
	Porosity	391	Gas measurement
	Permeability	386	Gas measurement
	Clay contents	61	X-ray diffraction
	Clay mineral components	25	X-ray diffraction
	Formation water salinity	18	Water analysis

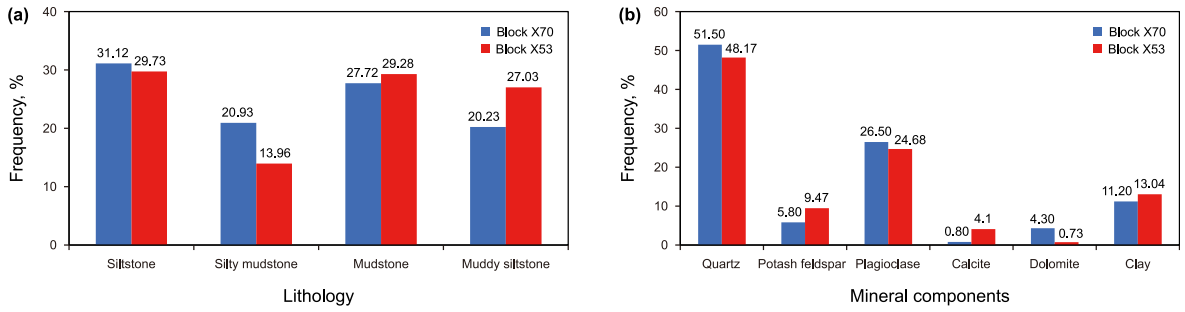

Fig. 1. Lithology **(a)** and mineral components **(b)** of the study area.

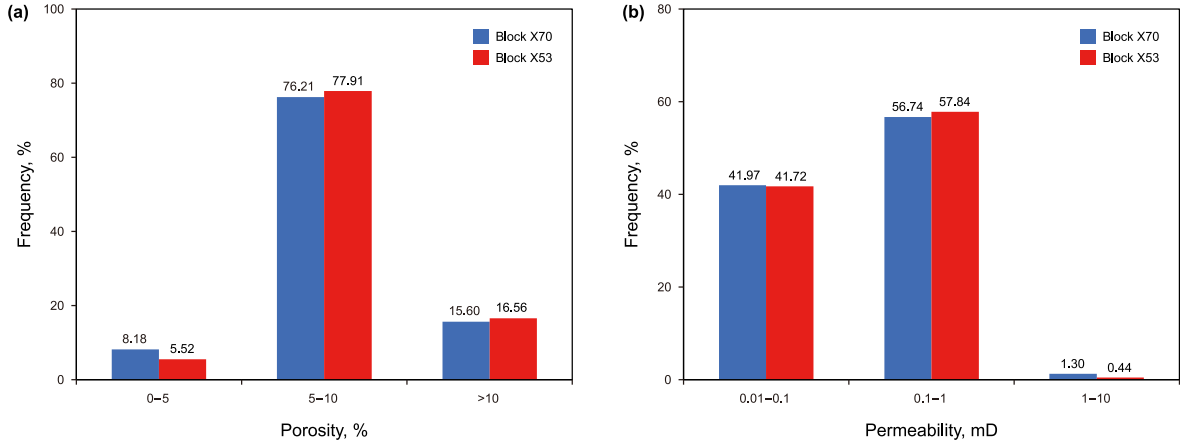

Fig. 2. Porosity **(a)** and permeability **(b)** of the study area.

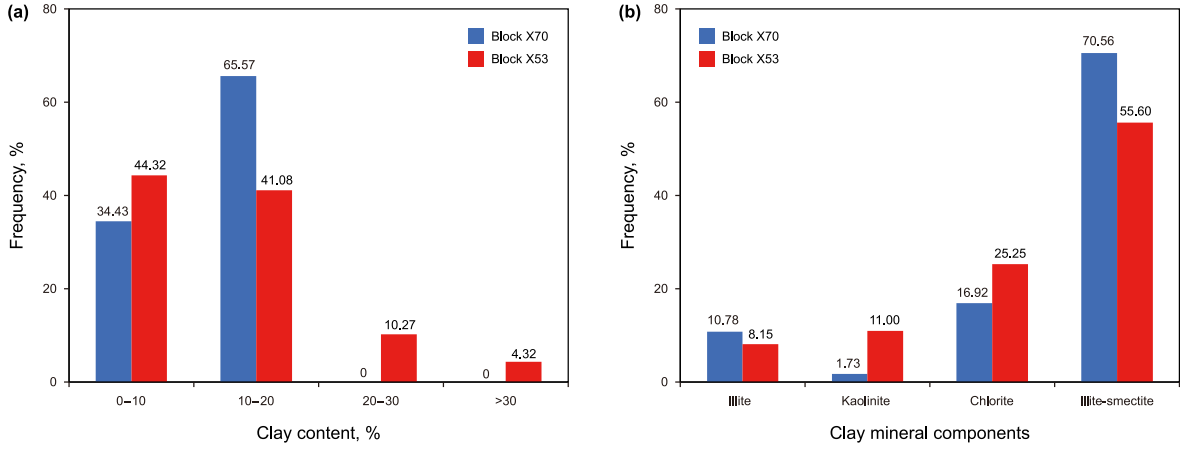

Fig. 3. Clay content **(a)** and clay mineral components **(b)** in the study area.

layer and the water layer.

In summary, the reservoirs in the study area have low porosity, low permeability, low oil and gas saturation, and low resistivity contrast. Thus, identifying the fluid and calculating oil and gas saturation prove to be challenging tasks.

3. Methods

3.1. Calculation of apparent formation water resistivity

Based on the Archie formula (Archie, 1942), the formation water resistivity in sandstone formations with complete water content is determined as follows:

$$R_w = R_0 \cdot \varphi^m \quad (1)$$

where R_0 is the resistivity of the water layer; φ is the porosity of sandstone; m is the cementation index; and R_w is the formation water resistivity. If the formation contains oil and gas, the formation resistivity R_t is used to replace R_0 in Eq. (1). The result is denoted as apparent formation water resistivity, R_{wa}, and is calculated as follows:

$$R_{wa} = R_t \cdot \varphi^m \quad (2)$$

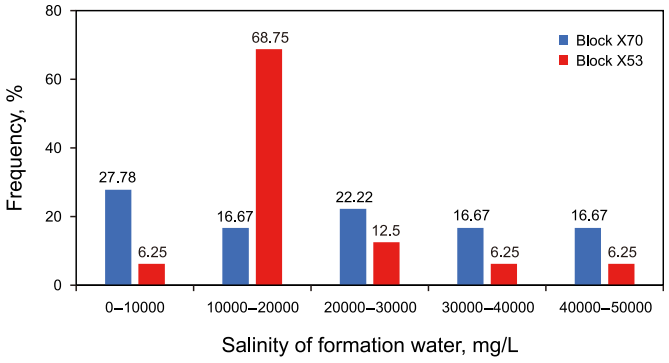

Fig. 4. Distribution of formation water salinity in the study area.

Parameter R_{wa} reflects the conductivity of reservoir fluid to some extent, and thus it is commonly used to identify fluid types in reservoirs. There are two main fluid identification methods based on R_{wa}. The first method directly compares the R_{wa} value. If the fluid in the reservoir is water, R_{wa} is small, and if the reservoir contains oil and gas, R_{wa} is large. The second method assumes that the $\sqrt{R_{wa}}$ of all logging depth points in the target layer follows a Gaussian distribution. The Gaussian distribution fitting result of $\sqrt{R_{wa}}$ is denoted as the apparent formation water resistivity spectrum, or the water spectrum for short. For oil and gas layers, $\sqrt{R_{wa}}$ is relatively dispersed and the water spectrum is wide and flat. For water layers, $\sqrt{R_{wa}}$ is relatively concentrated, and the water spectrum shape is narrow and sharp. Thus, the water spectrum can be used to identify the fluid types, denoted as the water spectrum method.

The reservoirs in the study area contain a large amount of shale, and thus the Archie formula is no longer applicable. To avoid the influence of shale, Simandoux (1963) proposed a method to calculate oil and gas saturation suitable for shaly sand formation, namely Simandoux formula, as shown in Eq. (3):

$$\frac{1}{R_t}=\frac{S_w V_{sh}}{R_{sh}}+\frac{\varphi^2 S_w^2}{aR_w} \tag{3}$$

where R_{sh} is the shale resistivity; V_{sh} is the shale content; and S_w is the water saturation. Eq. (3) regards formation resistivity R_t as the result of the parallel conduction between the shale and sandstone components.

Based on the Simandoux formula, Poupon and Leveaux proposed the Indonesia formula, as described in Eq. (4) (Poupon and Leveaux, 1971):

$$\frac{1}{\sqrt{R_t}}=\left(\frac{V_{sh}^d}{\sqrt{R_{sh}}}+\frac{\varphi^{m/2}}{\sqrt{aR_w}}\right)S_w^{n/2} \tag{4}$$

In practical applications, it is typically assumed that the values of a and d are 1, and the values of m and n are 2. The left and right sides of the Indonesia formula are in the form of square roots, indicating that the conductivity of the formation depends on the conductivity of the formation water network, the conductivity of the shale network, and the additional conductivity generated by the cross-linking of the two networks.

Let $S_w = 1$, then $R_{wa} = R_w$, then Eq. (4) can be simplified as

$$R_{wa}=\frac{\varphi^2}{\left(\frac{1}{\sqrt{R_t}}-\frac{V_{sh}}{\sqrt{R_{sh}}}\right)^2} \tag{5}$$

Eq. (5) appears to be suitable for the apparent formation water resistivity calculation of shaly sand formation. However, in reality, this is not feasible. The result of Eq. (5) may be extremely large, or even infinite, which is not suitable for the derivation of the water spectrum. Thus, it is critical to analyze the underlying reasons for this phenomenon and improve the model of apparent formation water resistivity calculations, which is the basis for the application of the water spectrum method to shaly sand formation.

The denominator on the right-hand-side of Eq. (5) consists of two components, namely, $1/\sqrt{R_t}$ and $V_{sh}/\sqrt{R_{sh}}$, which represent the reservoir conductivity and the conductivity of the shale component of the reservoir, respectively. When the values of these two components are close, the denominator on the right side of the Eq. (5) is small, resulting in an extremely large R_{wa} value. This indicates that when the conductivity of the reservoir is close to that of the shale part, the conductivity of the reservoir almost entirely comes from the shale component. The sandstone component is almost non-conductive compared to that of the shale, and R_{wa} is extremely large even infinite. There is no constraint between V_{sh} and R_t in Eq. (5), and the case where $1/\sqrt{R_t}$ is close to $V_{sh}/\sqrt{R_{sh}}$ does not necessarily have physical significance. Moreover, R_{wa} in Eq. (5) only represents the R_{wa} of the sandstone component. In fact, R_{wa} is the result of the parallel conduction of the shale and sandstone components, and thus should not be extremely large or infinite as the R_{wa} of the shale component is typically a limited, small value.

In this paper, the reservoir resistivity R_t and shale volume V_{sh} are used as independent variables for numerical simulations. According to the actual situation of the study area, the shale component resistivity of the formation is set to 4 Ω·m, and the porosity is set to 10%. Fig. 5(a) presents the simulation results based on the Indonesia formula, where the x-axis represents reservoir resistivity R_t, the y-axis represents the shale content V_{sh}, and the z-axis represents apparent formation water resistivity R_{wa}. When the shale content exceeds 20%, the R_{wa} derived from the Indonesia formula may be extremely large, and is no longer applicable for the water spectrum estimation.

Given this phenomenon, this paper proposes a new model for calculating apparent formation water resistivity, as shown in Eq. (6):

$$R_{wa}=R_t\cdot\varphi^m\cdot e^{V_{sh}} \tag{6}$$

Eq. (6) is an improvement of Eq. (2). The term $e^{V_{sh}}$ is added to compensate for the influence of the shale's additional conductivity on R_{wa}. The compensation term $e^{V_{sh}}$ increases with V_{sh}, indicating that the higher the shale content, the greater the impact on R_{wa}, and the greater the required compensation. When $V_{sh} = 0$, $e^{V_{sh}} = 1$, implying that the reservoir is a sandstone reservoir. For this case, R_{wa} does not require compensation, and Eq. (6) is equal to Eq. (2). The numerical simulation is carried out based on Eq. (6), and Fig. 5(b) depicts the simulation results, where the x-axis represents R_t, the y-axis represents V_{sh}, and the z-axis represents R_{wa}. The parameter R_{wa} increases gradually with V_{sh} and R_t, and the maximum of R_{wa} does not exceed 2 Ω·m. This avoids the occurrence of abnormal values. The proof of Eq. (6) is detailed in Appendix A.

3.2. Calculation of oil and gas saturation

According to the Archie formula, we have

$$\frac{R_t}{R_w}=\frac{ab}{S_w^n\varphi^m} \tag{7}$$

Let $a = 1$, $b = 1$, then Eq. (7) can be expressed as

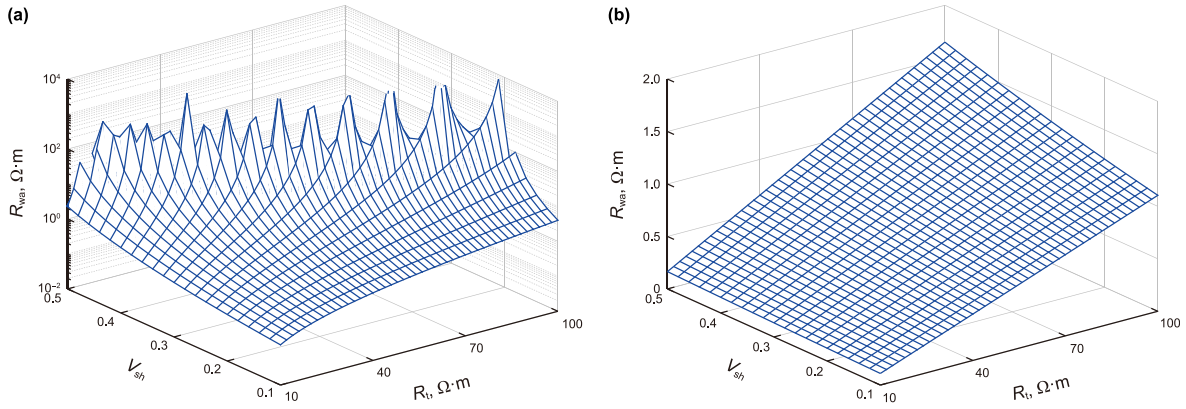

Fig. 5. **(a)** Results simulated based on the Indonesia model; **(b)** results simulated based on the new model.

$$S_w = \sqrt[n]{\frac{R_w}{R_t \varphi^m}} \tag{8}$$

Based on Eqs. (2) and (8), we can get

$$S_w = \sqrt[n]{R_w / R_{wa}} \tag{9}$$

where n is the saturation index in the Archie formula. Assuming that the number of logging depth sampling points of a reservoir is k, the average water saturation of this reservoir can be expressed as

$$S_w = \left(\sqrt[n]{\frac{R_w}{R_{wa1}}} + \sqrt[n]{\frac{R_w}{R_{wa2}}} + \sqrt[n]{\frac{R_w}{R_{wa3}}} + \cdots\cdots \sqrt[n]{\frac{R_w}{R_{wak}}} \right) \Bigg/ k = \sum_{i=1}^{k} \sqrt[n]{\frac{R_w}{R_{wai}}} \Bigg/ k \tag{10}$$

where R_{wai} (i = 1, 2, 3, …, k) represents the apparent formation water resistivity at the ith depth sampling point of the reservoir. Eq. (10) can be simplified as

$$S_w = \sqrt[n]{R_w} \left(\frac{1}{\sqrt[n]{R_{wa1}}} + \frac{1}{\sqrt[n]{R_{wa2}}} + \frac{1}{\sqrt[n]{R_{wa3}}} + \cdots\cdots + \frac{1}{\sqrt[n]{R_{wak}}} \right) \Bigg/ k = \sqrt[n]{R_w} \sum_{i=1}^{k} \frac{1}{\sqrt[n]{R_{wai}}} \Bigg/ k \tag{11}$$

Assuming that $\sqrt{R_{wa}}$ follows a Gaussian distribution, then the Gaussian distribution of $\sqrt{R_{wa}}$ is expressed as

$$f(x) = \frac{1}{\sqrt{2\pi}\sigma} \exp\left(-\frac{(x-\mu)^2}{2\sigma^2} \right) \tag{12}$$

where x represents $\sqrt{R_{wa}}$; $f(x)$ is the probability density; and μ and σ are the average and standard deviation of $\sqrt{R_{wa}}$, respectively. Let

$$y = \frac{1}{\sqrt[n]{x^2}} \tag{13}$$

then the distribution of y is expressed as follows:

$$g(y) = \frac{|-n/2| \cdot y^{-(n/2+1)}}{\sqrt{2\pi}\sigma} \exp\left(-\frac{(y^{-n/2} - \mu)^2}{2\sigma^2} \right) \tag{14}$$

where $g(y)$ is probability density. Combine Eqs. (14) and (11) results in the following:

$$S_w = \sqrt[n]{R_w} E(y) \tag{15}$$

where $E(y)$ represents the expectation of the distribution as shown in Eq. (14). It can be observed from Eq. (14) that $E(y)$ is related to μ and σ. Therefore, the average and standard deviation of $\sqrt{R_{wa}}$ can be used to calculate saturation.

In order to accurately calculate the oil and gas saturation, in addition to the average and standard deviation of the water spectrum, we also introduce two endpoints of the water spectrum (minimum and maximum values of $\sqrt{R_{wa}}$). Fig. 6 presents an example simulated water spectrum to illustrate the shortcomings of using only the average and standard deviation of the water spectrum for its characterization. For $\sqrt{R_{wa}}$ values less than 0, the corresponding probability is not 0 (dotted red line in Fig. 6), which is impossible in reality. Negative values of $\sqrt{R_{wa}}$ have no actual physical meaning. By introducing endpoints, the water spectrum can be more accurately characterized, and the range of $\sqrt{R_{wa}}$ can be determined. The oil and gas saturation can be calculated by using four parameters obtained from the water spectrum: average, standard deviation, left endpoint, and right endpoint.

We mark the left and right endpoints of the water spectrum as ep_l and ep_r. The linear regression method is used to establish a

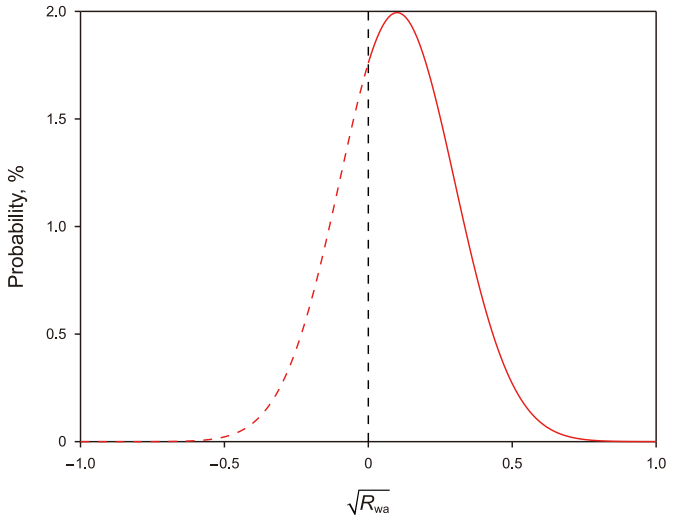

Fig. 6. Distribution of $\sqrt{R_{wa}}$.

model for calculating oil and gas saturation S_o, which is formulated as follows:

$$S_o = const_a \cdot \mu + const_b \cdot \sigma + const_c \cdot ep_l + const_d \cdot ep_r + const_e \quad (16)$$

where $const_a$, $const_b$, $const_c$, $const_d$, and $const_e$ are constants. Note that the endpoint positions are not required to be considered in the qualitative fluid identification of reservoirs using the water spectrum, yet they are important parameters in the calculation of oil and gas saturation.

The model of calculating oil and gas saturation using the average and standard deviation of the water spectrum is denoted as the "double-parameter" model, and the model of calculating oil and gas saturation using the average, standard deviation, and endpoints of the water spectrum is denoted as the "four-parameter" model.

4. Results

4.1. Calculation of apparent formation water resistivity

Reservoir No. 1 of Well X53-3 in block X53 is used to compare the proposed model with the Indonesia formula for calculating apparent formation water resistivity by processing actual logging data. As shown in Fig. 7, the first track is the formation depth. The second track includes the borehole diameter logs (CAL), natural gamma logs (GR), and spontaneous potential logs (SP). The third track includes the deep lateral resistivity logs (RLLD) and shallow lateral resistivity logs (RLLS). The fourth track includes the neutron logs (CNL), acoustic interval transit time logs (AC), and density logs (DEN). The fifth track includes R_{wa} obtained by the Indonesia formula (R_{wa}_Indonesia) and the new model (R_{wa}_New). The sixth track includes the oil test results. Fig. 7 reveals that the R_{wa} calculated by the Indonesia formula have extremely large values on multiple occasions, and the new model effectively avoids this problem.

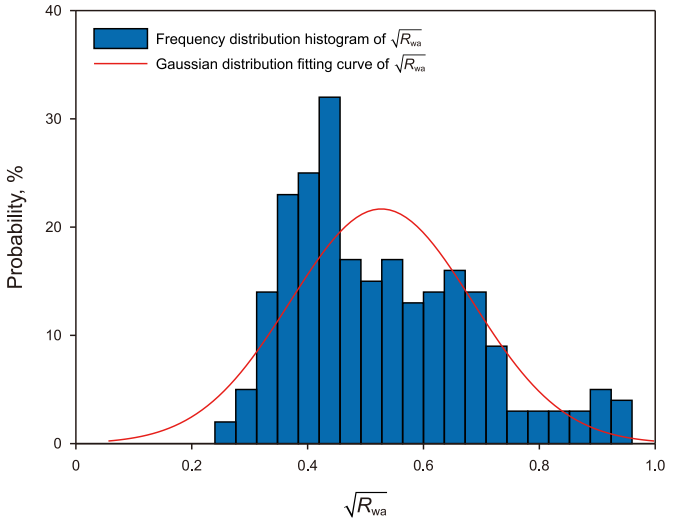

Fig. 8. Frequency distribution histogram and Gaussian distribution fitting curve of $\sqrt{R_{wa}}$ of No.1 reservoir in Well X53-3.

4.2. Fluid identification

The top and bottom depths of reservoir No. 1 of well X53-3 are 1981.8 m and 2005.4 m, respectively. The depth sampling interval is 0.1 m, with a total of 237 depth sampling points. The proposed model is used to calculate the $\sqrt{R_{wa}}$ of these depth sampling points. Fig. 8 presents the calculated distribution of $\sqrt{R_{wa}}$ (histogram). Assuming $\sqrt{R_{wa}}$ follows a Gaussian distribution, the Gaussian distribution fitting curve (red line) is also indicated in Fig. 8. The water spectrum of reservoir No.1 is observed to be relatively wide. According to regional observations, there is no oil layer in the study area. Therefore, reservoir No.1 of Well X53-3 is determined to be an

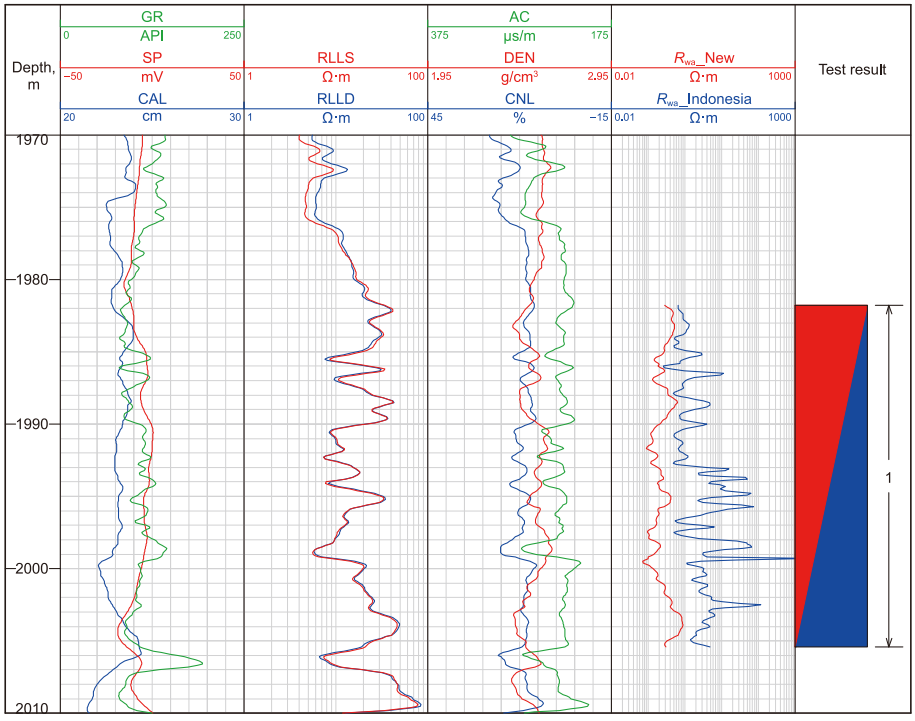

Fig. 7. Comparison of two models for calculating apparent formation water resistivity.

oil-water layer, which matches the test result.

We counted the data of 13 layers belonging to 8 wells in block X53, including 6 water layers and 7 oil-water layers. Table 2 reports the deep lateral resistivity data of these layers. The difference between the average deep lateral resistivity of the water layers and that of oil-water layers is not obvious. The $\sqrt{R_{wa}}$ of these layers is calculated and used to construct the water spectrum Fig. 9(a). The blue lines represent the water spectra of the water layers, and the red lines represent the water spectra of the oil-water layers. In order to clearly reveal the difference between the water spectra among layers, we counted the average and standard deviation of these water spectra in Fig. 9(b), where the *x*-axis and *y*-axis represent the average and standard deviation of the water spectrum, respectively. The red circles denote the oil-water layers, and the blue triangles represent the water layers.

We counted the data of 8 layers belonging to 8 wells in block X70, including 4 water layers and 4 oil-water layers. Table 3 reports the deep lateral resistivity data of these layers. The water spectra of these layers are shown in Fig. 10(a), while the average and standard deviation of these water spectra are depicted in Fig. 10(b). For Fig. 10(a), the blue lines represent the water spectra of the water layers, and the red lines represent the water spectra of the oil-water layers. In Fig. 10(b), the red circles denote the oil-water layers, and the blue triangles denote the water layers.

Figs. 9(a) and 10(a) reveal that the water spectra of the water layers are narrower than those of the oil-water layers. It can be seen from Figs. 9(b) and 10(b) that although the average of the water spectrum of the oil-water layer is not necessarily larger than that of the water layer, the standard deviation of the former is generally larger than that of the latter. These results are in agreement with the analysis in the "Methods" section. More specifically, the water spectrum of oil-bearing layers is broader, with a larger standard deviation than that of the water layers. Therefore, the standard deviation can serve as a criterion for fluid identification. For the two study blocks, a standard deviation of 0.1 serves as the classification boundary. Layers with a standard deviation of the water spectrum greater than 0.1 can be classified as oil-water layers, while layers with a standard deviation of the water spectrum less than 0.1 can be classified as water layers. Among the 13 layers in block X53, only one water layer does not conform to the above laws. Similarly, among the 8 layers in block X70, only one oil-water layer does not conform to the above laws. The results prove the effectiveness of the water spectrum method in fluid identification.

4.3. Oil and gas saturation calculation

4.3.1. Numerical simulation

In order to verify the model of oil and gas saturation calculation proposed in this paper, six layers are simulated, as shown in Fig. 11. The first subplot in Fig. 11 (with legend "$S_w = 0.35$") is taken as an example to explain Fig. 11 in detail. In particular, it represents a layer containing 100 depth sampling points, corresponding to water saturation variations ranging from 0.3 to 0.4, with an average water saturation of 0.35. The remaining subplots are similar. The average water saturation of the six layers is 0.35, 0.45, 0.55, 0.65, 0.75 and 0.85, respectively. These layers can form one or more heterogeneous and complex reservoirs. In the simulation, the variation range of shale content is 10%–20%, while the formation water resistivity varies from 0.1 Ω·m to 1 Ω·m. The porosity is 10% and the noise level of the resistivity is 10%. These simulation conditions are essentially in line with the actual situation of the study area. As the formation water resistivity in the study area is difficult to calculate, the average formation water resistivity is used for the Indonesia formula. The four-parameter model, double-parameter model and Indonesia formula are used for oil and gas saturation calculation of the simulated layers. Fig. 12 presents the simulation results.

The *x*-axis in Fig. 12(a) and (b) represent the simulation number. The *y*-axis in Fig. 12(a) denotes the determination coefficient (R^2) of the simulation results, while that of the *y*-axis in Fig. 12(b) is the root mean square error (RMSE). The red, blue and black dots and lines represent the simulation results of the four-parameter model, double-parameter model, and Indonesia formula, respectively. We conducted a total of 100 simulations (Table 4). As shown in Fig. 12, the four-parameter model is superior to the double-parameter model, while the double-parameter model is superior to the Indonesia formula.

4.3.2. Practical application

The four-parameter model, double-parameter model, and Indonesia formula are used to process the actual data in the study area.

Blocks X53 and X70 have 124 and 97 cores with oil saturation experimental data, respectively. The data were obtained by the distillation extraction method. The cores from both blocks belong to 6 layers, respectively. Tables 5 and 6 report the water spectrum parameters and oil saturation measurement results, while Figs. 13 and 14 present the results of oil saturation calculation for blocks X53 and X70, respectively.

In Figs. 13 and 14, the *x*-axis denotes the calculated oil saturation, while the *y*-axis represents the measured oil saturation, which is the average of oil saturation measurement results of cores belonging to the same layer. The black triangles denote the results calculated by the Indonesia formula, the red circles represent the results calculated by the four-parameter model, and the blue squares indicate the results calculated by the double-parameter

Table 2
Statistics of deep lateral resistivity of layers in the X53 block.

Layer type	Layer number	Minimum value, Ω·m	Maximum value, Ω·m	Average, Ω·m
Water layer	1	5.73	93.26	23.27
	2	14.22	20.36	17.71
	3	17.30	25.67	23.64
	4	13.38	24.63	18.96
	5	14.71	33.97	22.04
	6	17.48	36.58	23.49
Oil-water layer	7	5.90	74.78	21.01
	8	5.81	49.44	20.96
	9	5.76	49.06	15.80
	10	5.29	65.14	18.56
	11	4.48	157.81	18.19
	12	4.97	86.16	22.69
	13	21.02	43.66	36.87

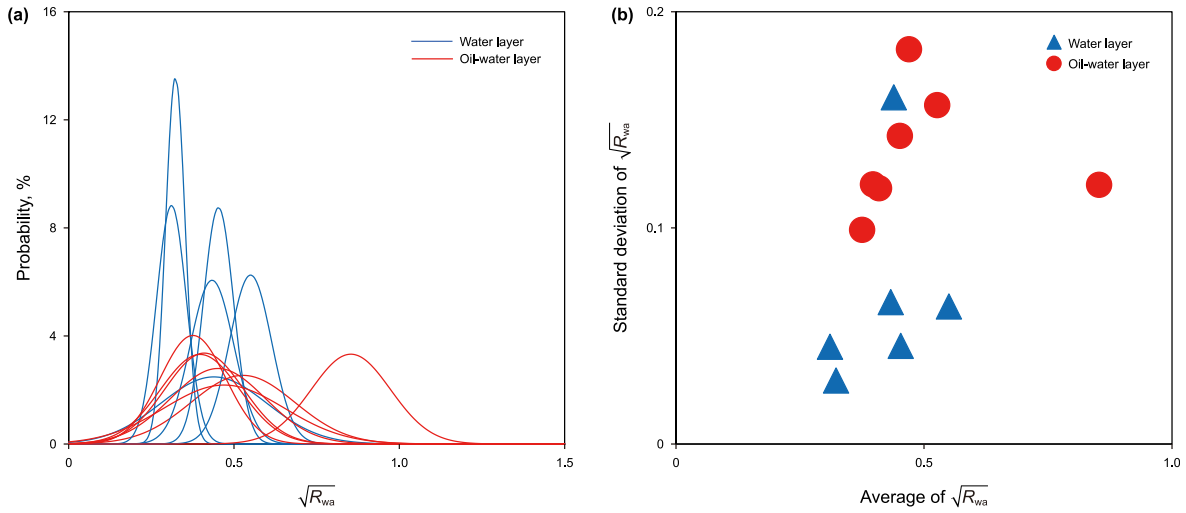

Fig. 9. **(a)** Water spectra of layers in the X53 block; **(b)** water spectra parameters in the X53 block.

Table 3
Statistics of deep lateral resistivity of layers in the X70 block.

Layer type	Layer number	Minimum value, Ω·m	Maximum value, Ω·m	Average, Ω·m
Water layer	1	6.36	56.26	25.59
	2	16.72	28.24	25.17
	3	16.23	21.28	18.98
	4	10.24	24.14	15.13
Oil-water layer	5	8.83	27.9	17.46
	6	9.23	60.23	25.73
	7	29.56	42.13	35.38
	8	7.84	63.92	25.79

model. The four-parameter model outperforms the double-parameter model and the Indonesia formula. This conclusion is consistent with the simulation results, which proves the effectiveness of the four-parameter model.

5. Discussions

5.1. R_{wa} calculation models

In this section, we analyze two other R_{wa} calculation models based on the Waxman-Smits and Thomas-Stieber models.

The Waxman-Smits model is shown in Eqs. (17) and (18) (Waxman and Smits, 1968):

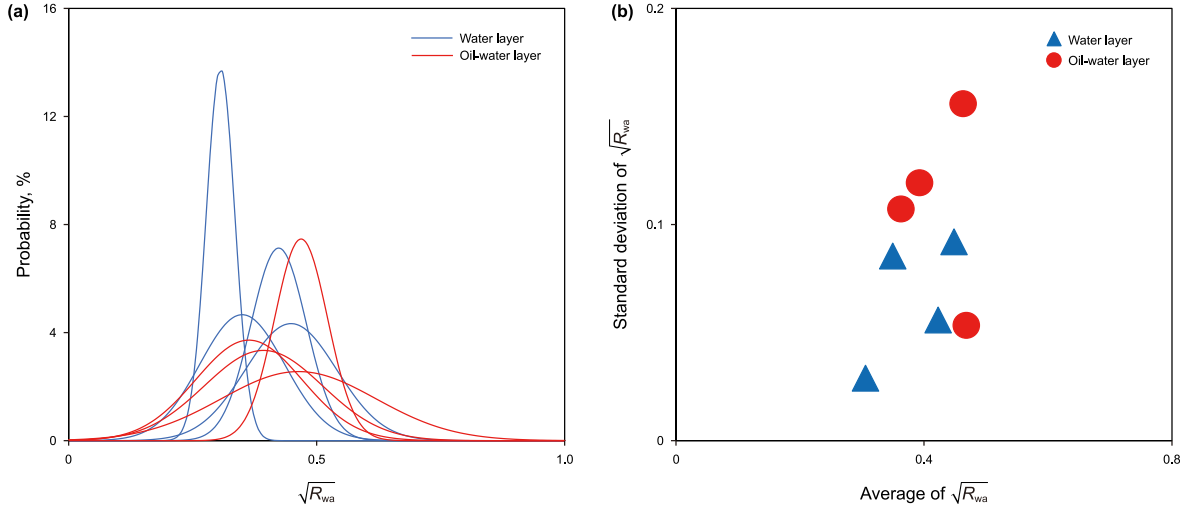

Fig. 10. **(a)** Water spectra of layers in the X70 block; **(b)** water spectra parameters in the X70 block.

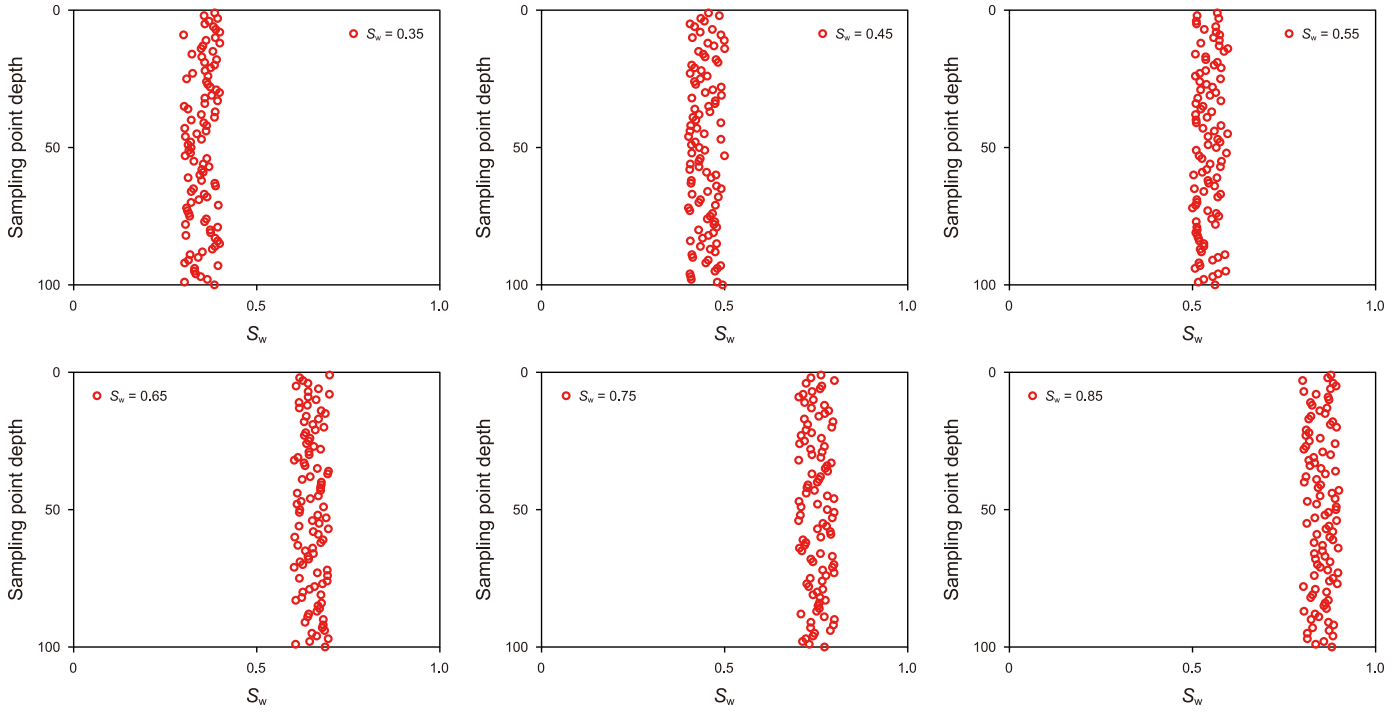

Fig. 11. Water saturation models.

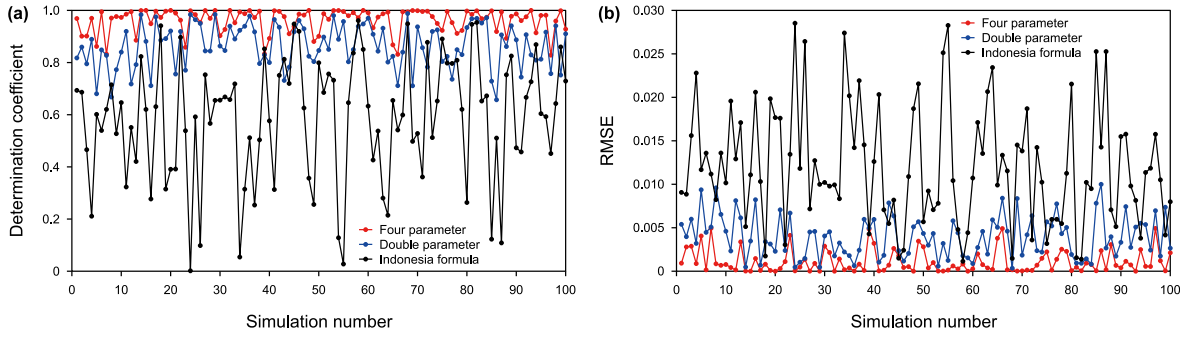

Fig. 12. Oil and gas saturation calculation results obtained by different models. **(a)** Determination coefficient (R^2) of the simulation results; **(b)** root mean square error (RMSE) of the simulation results.

Table 4
Average value of 100 simulation results.

Model	R^2	RMSE
Four-parameter	0.96	0.0011
Double-parameter	0.86	0.0040
Indonesia formula	0.58	0.0121

$$\frac{1}{R_t}=\frac{S_{wt}^{n^*}}{F^*}\left(\frac{1}{R_w}+BQ_v\Big/S_{wt}\right) \tag{17}$$

$$B=3.83\left(1-0.83e^{-\frac{1}{2R_w}}\right) \tag{18}$$

where Q_v is the cation-exchange capacity, B is the exchanged-cation equivalent conductivity, F^* is the shaly sand formation resistivity

Table 5
Water spectrum parameters and oil saturation measurement results in the X53 block.

Number	Average	Standard deviation	Left endpoint	Right endpoint	Oil saturation, %
1	0.59	0.095	0.43	0.74	22.7
2	0.69	0.101	0.58	0.82	29.4
3	0.41	0.101	0.23	0.52	23.9
4	0.55	0.073	0.40	0.61	16.6
5	0.57	0.069	0.50	0.65	13.4
6	0.60	0.117	0.32	1.01	24.5

Table 6
Water spectrum parameters and oil saturation measurement results in the X70 block.

Number	Average	Standard deviation	Left endpoint	Right endpoint	Oil saturation, %
1	0.40	0.043	0.35	0.45	16.3
2	0.36	0.100	0.25	0.51	14.2
3	0.44	0.065	0.33	0.56	9.0
4	0.38	0.042	0.26	0.43	22.6
5	0.36	0.049	0.24	0.46	17.0
6	0.58	0.084	0.28	0.65	18.1

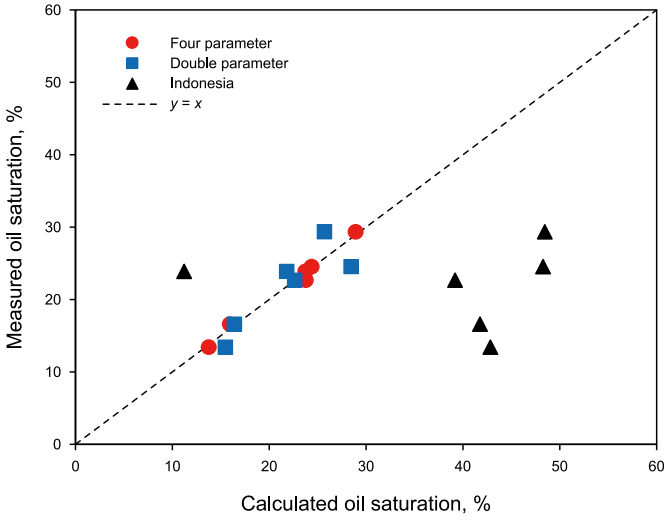

Fig. 13. Practical application effect in the X53 block.

factor, and n^* is the saturation index of clay-free formation, usually set n^* to 2. Combine Eqs. (17) and (18), let $S_{wt} = 1$, then we can get

$$R_{wa} = 1 \Big/ \left(F^* \Big/ R_t - 3.83\left(1 - 0.83e^{-\frac{1}{2R_{wa}}}\right)Q_v\right) \tag{19}$$

Eq. (19) is an implicit function, and R_{wa} is difficult to calculate. In addition, Q_v needs to be obtained by core experimental, which limits the application of the Waxman-Smits model.

According to the Thomas-Stieber model, the volume of laminar shale can be calculated by the following equation (Ghaleh et al., 2017; El-Sayed, 2020):

$$V_{lam} = \frac{\varphi_t - \varphi_{max} + V_{sh}(1 - \varphi_{sh})}{1 - \varphi_{max}} \tag{20}$$

where V_{lam} is the volume of laminar shale, φ_t is the total porosity, φ_{max} is the clean sand porosity, and φ_{sh} is the shale porosity. The effective porosity φ_{esd} and the volume of sand V_{sd} can be calculated by Eqs. (21) and (22):

$$\varphi_{esd} = \frac{\varphi_t - (V_{sh}\varphi_{sh})}{1 - V_{lam}} \tag{21}$$

$$V_{sd} = 1 - V_{lam} \tag{22}$$

The resistivity of sandstone R_{sd} can be obtained according to Poupon et al. (1954):

$$\frac{1}{R_t} = \frac{V_{sh}}{R_{sh}} + \frac{V_{sd}}{R_{sd}} \tag{23}$$

According to the Archie formula, we can obtain

$$S_{w\_sd} = \sqrt[n]{\frac{aR_w}{\varphi_{esd}^m R_{sd}}} \tag{24}$$

Let $n = m = 2$; $a = 1$; $S_{w\_sd} = 1$, we can obtain

$$R_{wa} = \varphi_{esd}^2 R_{sd} = \frac{\varphi_{esd}^2 V_{sh}}{\left(\frac{1}{R_t} - \frac{V_{sh}}{R_{sh}}\right)} \tag{25}$$

Eq. (25) has similarity with Eq. (5). When $1/R_t$ is close to V_{sh}/R_{sh}, the result of Eq. (25) may be extremely large or even infinite. Let $\varphi_{esd} = 1$, $R_{sh} = 4\ \Omega\cdot m$, the simulation results are shown in Fig. 15. It

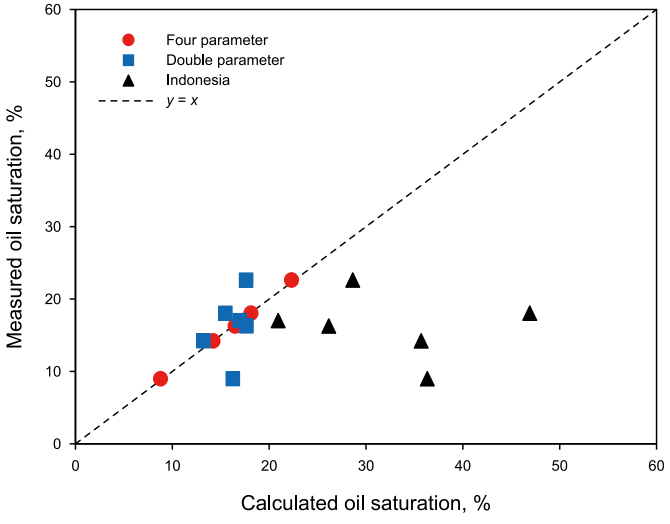

Fig. 14. Practical application effect in the X70 block.

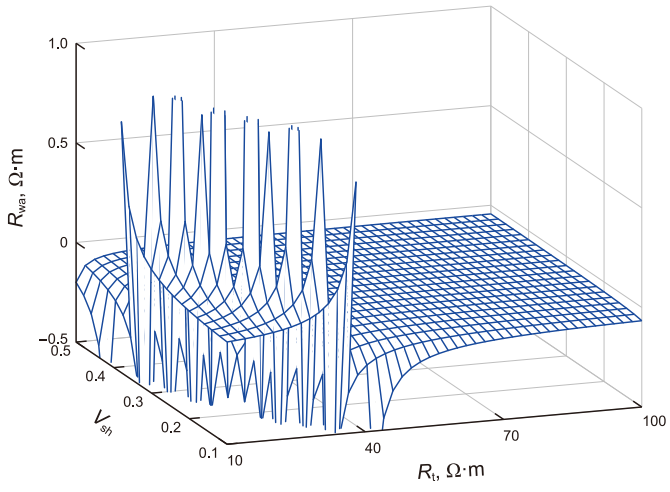

Fig. 15. Results simulated based on the Thomas-Stieber model.

can be observed that R_{wa} may be extremely large or negative.

In summary, the Waxman-Smits model and the Thomas-Stieber model are not suitable for calculating R_{wa}, and the model shown in Eq. (6) is more simple and reliable.

5.2. Saturation calculation models

In Section 4.3.2, we demonstrated that the Indonesia model cannot accurately evaluate the oil saturation in the study area. In this section, we apply two additional models, the Waxman-Smits and Thomas-Stieber models to calculate the oil saturation in the study area. Fig. 16(a) and (b) show the results of different models for blocks X53 and X70, respectively. In Fig. 16, the green triangles represent the results of the Thomas-Stieber model and the purple squares represent the results of the Waxman-Smits model.

In block X53, the R^2 for the Thomas-Stieber model results and core experimental data is 0.70, and that of the Waxman-Smits model is 0.41. In block X70, the R^2 for the Thomas-Stieber model results and core experimental data is 0.22, and that of the Waxman-Smits model is 0.07. Fig. 16 indicates that the four-parameter model is more effective than the Waxman-Smits and Thomas-Stieber models in calculating the oil saturation in the study area.

For the four-parameter model, the average, standard deviation, and two endpoints of the water spectrum are used to calculate the oil saturation of reservoirs. To some extent, Fan et al. (2019) supports our findings. The authors determined the average and standard deviation magnitudes of the water spectrum of different types of layers to exhibit the following trend (from smallest to largest): water layer, oil-water layer and oil layer. This reveals that the average and standard deviation of the water spectrum are correlated with oil saturation. However, Fan et al. (2019) did not analyze the quantitative relationship between the average, standard deviation, and oil saturation, nor did they introduce endpoint values as parameters for the evaluation of oil saturation.

Traditional models for oil and gas saturation evaluations in shaly sand reservoirs require numerous parameters, namely, R_t, V_{sh}, R_{sh}, φ, R_w, m, and n for the Indonesia formula; R_t, V_{sh}, R_{sh}, φ, R_w, m, n, φ_{max}, and φ_{sh} for the Thomas-Stieber model; and R_t, φ, R_w, F^*, n^*, B, and Q_v for the Waxman-Smits model.

Among the above parameters, R_t and R_{sh} are affected by logging instrument errors, parameters V_{sh}, φ_{max}, and φ_{sh} are affected by model calculation errors, and parameters R_w, m, n, F^*, n^*, B, and Q_v are affected by experimental errors. In addition, limited laboratory data may not be suitable for the logging evaluation of the whole block. For example, for study areas with complex distributions of formation water salinity, it is difficult to determine the formation water resistivity of each reservoir.

The accumulated errors impact the application effect of traditional models. The four-parameter model only requires the average, standard deviation, and two endpoints of the water spectrum obtained by four parameters: R_t, φ, V_{sh}, and m. This reduces the error superposition.

The models proposed in this paper consider the influence of the additional conductivity of shale on the reservoir resistivity, which is particularly suitable for shaly sand reservoirs. If the reservoir resistivity is also affected by other factors, such as conductive minerals in the rock matrix, the application effect of the models proposed in this paper will be affected. For different factors affecting the reservoir resistivity, we suggest that when using the proposed models, the corresponding compensation component should be added to Eq. (6) to compensate for the reduction of reservoir resistivity.

6. Conclusions

In this paper, a new method is proposed for fluid identification and saturation calculations in low contrast tight sandstone reservoirs. The main contributions of this paper are as follows: Firstly, the shortcomings of the Indonesia, Waxman-Smits, and Thomas-Stieber models in calculating the apparent formation water resistivity of shaly sandstone are analyzed for the first time. Secondly, a new model for calculating the apparent formation water resistivity is constructed. Thirdly, a water spectrum method suitable for low contrast tight sandstone fluid identification is then developed, and a four-parameter model for the oil and gas saturation based on the water spectrum average, standard deviation, and two endpoints is subsequently established. Through the numerical simulations and actual data processing, the following conclusions are drawn:

(1) For R_{wa} calculations, the commonly used Indonesia, Thomas-Stieber and Waxman-Smits models may lead to abnormal values. The calculation model of R_{wa} proposed in this paper is simple and reliable, compensates for the influence of shale additional conductivity on R_{wa}, and avoids the occurrence of abnormal values.

(2) For the study area, the fluid types can be identified by the shape of the water spectrum. The water spectrum of the oil-water layer is wide and flat, and that of the water layer is narrow and sharp. The average of the water spectrum of the oil-water layer does not differ greatly from that of the water layer, yet the standard deviation of the water spectrum of the

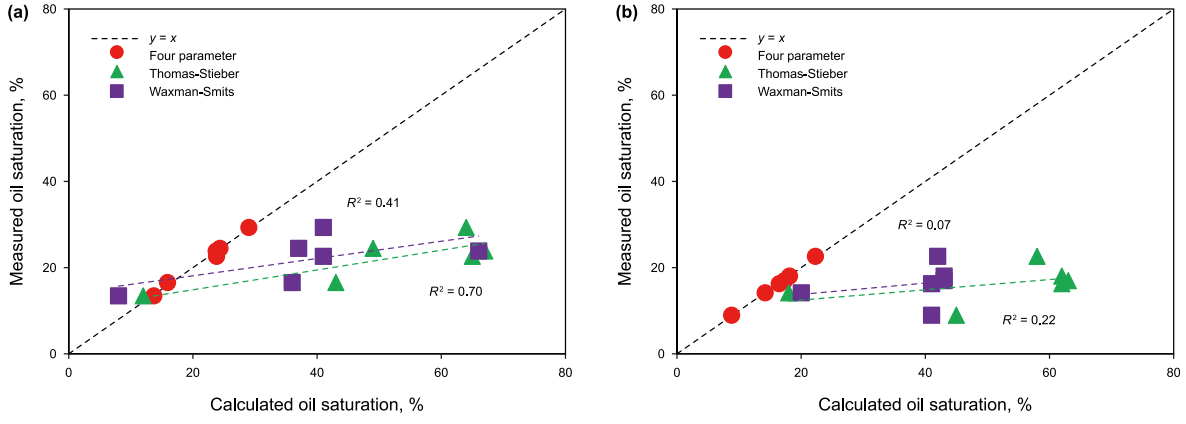

Fig. 16. The application effects of the Waxman-Smits model and the Thomas-Stieber model in the X53 block **(a)** and X70 block **(b)**.

oil-water layer is generally larger than that of the water layer. The standard deviation of the water spectrum in the water layer is generally less than 0.1, while the standard deviation of the water spectrum in the oil-water layer typically exceeds 0.1.

(3) For the study area, the oil saturation of low contrast tight sandstone reservoirs calculated by the four-parameter model is consistent with the core experimental results, while the results of the Thomas-Stieber, Waxman-Smits, and Indonesia model present large errors. The superior performance of the four-parameter model is attributed to the reduction of error superposition.

(4) The water spectrum method and four-parameter model proposed in this paper avoid errors caused by artificial reading and multi-layer joint tests. These methods are suitable for old well rechecking based on conventional logging data.

(5) The study primarily focuses on the influence of shale content on reservoir resistivity and provides limited coverage of the other genesis of low contrast reservoirs. Future research should focus on establishing corresponding models for calculating the apparent formation water resistivity based on different causes of low contrast reservoirs and further validating the effectiveness of the water spectrum method and the four-parameter model.

Nomenclature

R_w	Formation water resistivity
R_0	Water layer resistivity
φ	Porosity
R_{wa}	Apparent formation water resistivity
R_t	Formation resistivity
R_{sh}	Shale resistivity
V_{sh}	Shale content
S_w	Water saturation
μ	Average of water spectrum
σ	Standard deviation of water spectrum
S_o	Oil and gas saturation
ep_l	Left endpoint of water spectrum
ep_r	Right endpoint of water spectrum
Q_v	Cation-exchange capacity
B	Exchanged-cation equivalent conductivity
F^*	Shaly sand formation resistivity factor
n^*	Saturation index of clay-free formation
V_{lam}	Volume of laminar shale
V_{sd}	Volume of sand
φ_t	Total porosity
φ_{max}	Clean sand porosity
φ_{sh}	Shale porosity
φ_{esd}	Effective porosity
R_{sd}	Sandstone resistivity

CRediT authorship contribution statement

Shuai Wang: Writing – original draft, Methodology, Formal analysis, Data curation. **Ran-Hong Xie:** Writing – review & editing, Supervision, Methodology. **Guo-Wen Jin:** Writing – review & editing. **Jiang-Feng Guo:** Writing – review & editing. **Li-Zhi Xiao:** Writing – review & editing.

Declaration of competing interest

The authors declare that they have no known competing financial interests or personal relationships that could have appeared to influence the work reported in this paper.

Acknowledgements

This work was funded by the National Natural Science Foundation of China (42174131).

Appendix A

This section is used to prove the defect of the Indonesia formula in calculating apparent formation water resistivity and the rationality of the model proposed in this paper.

Starting from the Eq. (5) in the main text, denominator on the right-hand-side of Eq. (5) is analyzed, as shown in Eq. (A.1):

$$\frac{1}{\sqrt{R_t}}-\frac{V_{sh}}{\sqrt{R_{sh}}}=\frac{\sqrt{R_{sh}}-V_{sh}\sqrt{R_t}}{\sqrt{R_tR_{sh}}} \tag{A.1}$$

When the result of the above fomula is equal to a small value, R_{wa} will be equal to an extremely large value. Assuming that there is a linear relationship between the shale component resistivity R_{sh} and the formation resistivity R_t in shaly sandstone, and this relationship is expressed as Eq. (A.2) (Poupon et al., 1954):

$$R_t = A \cdot R_{sh} \tag{A.2}$$

Then the Eq. (A.1) can be rewritten as the Eq. (A.3), assuming that the equation is less than a small value $\tau = 0.001$:

$$\frac{1}{\sqrt{R_t}}-\frac{V_{sh}}{\sqrt{R_{sh}}}=\frac{1-V_{sh}\sqrt{A}}{\sqrt{AR_{sh}}}\le\tau \tag{A.3}$$

According to the regional situation, and in order to facilitate the calculation, set $A = 9$, $R_{sh} = 4\ \Omega\cdot$m, and then the above equation is expressed as Eq. (A.4):

$$V_{sh} \ge (1-0.006)/3 \tag{A.4}$$

According to the above equation, when the porosity is 10% and the shale content is more than 30%, the R_{wa} derived from the Indonesia formula will be more than 10000 $\Omega\cdot$m, which illustrates the defect of the Indonesia formula in calculating apparent formation water resistivity.

It is assumed that the relationship between shale component resistivity R_{sh} and formation water resistivity R_w satisfies Eq. (A.5):

$$R_{sh} = B \cdot R_w \tag{A.5}$$

Based on Eq. (A.5) and Eq. (5) in the main text, we get

$$R_{wa} = R_t\left(\frac{V_{sh}^2}{B^2}+\varphi^2+2\varphi\frac{V_{sh}}{B}\right) \tag{A.6}$$

where R_{wa} is the apparent formation water resistivity calculated by the Indonesia formula, and the result calculated by Eq. (6) in the main text is expressed as R_{wa}^*, then Eq. (A.7) is obtained:

$$\frac{R_{wa}^*}{R_{wa}}=\frac{e^{V_{sh}}}{\frac{V_{sh}^2}{\varphi^2B^2}+1+2\frac{V_{sh}}{\varphi B}}=\frac{e^{V_{sh}}}{\left(\frac{V_{sh}}{\varphi B}+1\right)^2} \tag{A.7}$$

According to the situation of the study area, let $\varphi = 10\%$, $R_w = 0.1\ \Omega\cdot$m, $R_{sh} = 4\ \Omega\cdot$m, then $B = 40$ (In fact, it is difficult to determine B due to the variation of formation water salinity). Fig. A.1 shows the relationship between R_{wa}^*/R_{wa} and shale content.

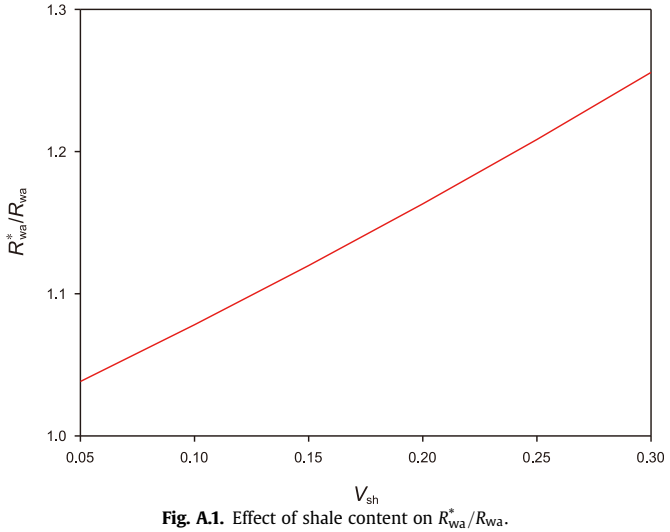

Fig. A.1. Effect of shale content on R^*_{wa}/R_{wa}.

In Fig. A.1, the *x*-axis represents shale content, and the *y*-axis represents R^*_{wa}/R_{wa} calculated by Eq. (A.7). As shown in Fig. A.1, the new method enlarges the apparent formation water resistivity actually, and the magnification effect increases with the increase of shale content, but it is always controlled in a small range, which proves the rationality of the proposed model.

References

Abudeif, A.M., Attia, M.M., Radwan, A.E., 2016. New simulation technique to estimate the hydrocarbon type for the two untested members of Belayim Formation in the absence of pressure data, Badri Field, Gulf of Suez, Egypt. Arabian J. Geosci. 9 (3), 218. https://doi.org/10.1007/s12517-015-2082-2.

Akkurt, R., Ahmad, N.A., Behair, A.M., et al., 2008. NMR radial saturation profiling for delineating oil-water contact in a high-resistivity low-contrast formation drilled with oil-based mud. In: SPWLA 49th Annual Logging Symposium. Austin, Texas.

Akkurt, R., Moore, M.A., Freeman, J.J., 1997. Impact of NMR in the development of a deepwater tuirbidite field. In: SPWLA 38th Annual Logging Symposium. Houston, Texas.

Akkurt, R., Vinegar, H.J., Tutunjian, P.N., et al., 1995. NMR logging of natural gas reservoirs. In: SPWLA 36th Annual Logging Symposium. Paris, France.

Archie, G.E., 1942. The electrical resistivity log as an aid in determining some reservoir characteristics. Trans. AIME 146 (1), 54–62. https://doi.org/10.2118/942054-g.

Bai, Z., Tan, M., Li, G., et al., 2019. Analysis of low-resistivity oil pay and fluid typing method of Chang 8_1 Member, Yanchang Formation in Huanxian area, Ordos Basin, China. J. Petrol. Sci. Eng. 175, 1099–1111. https://doi.org/10.1016/j.petrol.2019.01.015.

Belevich, A., Bal, A.A., 2017. The problem with silt in low resistivity low contrast pay reservoirs. In: SPWLA 58th Annual Logging Symposium. Oklahoma, USA.

Coates, G.R., Gardner, J.S., Miller, D.L., 1994. Applying pulse-echo NMR to shaly sand formation evaluation. In: SPWLA 35th Annual Logging Symposium. Oklahoma, USA.

Clavier, C., Coates, G., Dumanoir, J., 1984. Theoretical and experimental bases for the dual-water model for interpretation of shaly sands. Soc. Petrol. Eng. J. 24 (2), 153–168. https://doi.org/10.2118/6859-pa.

Das, B., Chatterjee, R., 2018. Well log data analysis for lithology and fluid identification in Krishna-Godavari Basin, India. Arabian J. Geosci. 11 (10), 1–12. https://doi.org/10.1007/s12517-018-3587-2.

El-Sayed, A.S., 2020. A novel method to improve water saturation in shaly sand reservoirs using wireline logs. J. Petrol. Sci. Eng. 185, 106602. https://doi.org/10.1016/j.petrol.2019.106602.

Fan, X., Wang, G., Dai, Q., et al., 2019. Using image logs to identify fluid types in tight carbonate reservoirs via apparent formation water resistivity spectrum. J. Petrol. Sci. Eng. 178, 937–947. https://doi.org/10.1016/j.petrol.2019.04.006.

Ghaleh, S.P., Taghizadeh, M., Far, E.R., et al., 2017. Evaluation of laminated shaly sand sequences in Ahwaz oil field using (via) Thomas Stieber method and conventional petrophysical logs. J. Petrol. Sci. Eng. 152, 564–574. https://doi.org/10.1016/j.petrol.2017.01.041.

Hamada, G.M., Al-Blehed, M.S., Al-Awad, M.N., et al., 2001. Petrophysical evaluation of low-resistivity sandstone reservoirs with nuclear magnetic resonance log. J. Petrol. Sci. Eng. 29 (2), 129–138. https://doi.org/10.1016/s0920-4105(01)00095-x.

Heaton, N., Bachman, H.N., Minh, C.C., et al., 2007. 4D NMR-applications of the radial dimension in magnetic resonance logging. In: SPWLA 48th Annual Logging Symposium. Austin, Texas.

He, M., Gu, H., Wan, H., 2020. Log interpretation for lithology and fluid identification using deep neural network combined with MAHAKIL in a tight sandstone reservoir. J. Petrol. Sci. Eng. 194, 107498. https://doi.org/10.1016/j.petrol.2020.107498.

Hingle, A.T., 1959. The use of logs in exploration problems. In: Society of Exploration Geophysicists, 29th Meeting.

Jain, V., Minh, C.C., Heaton, N., et al., 2013. Characterization of underlying pore and fluid structure using factor analysis on NMR data. In: SPWLA 54th Annual Logging Symposium. New Orleans, Louisiana.

Koelman, J.M.V.A., De Kuijper, A., 1997. An effective medium model for the electric conductivity of an N-component anisotropic and percolating mixture. Phys. Stat. Mech. Appl. 247 (1–4), 10–22. https://doi.org/10.1016/s0378-4371(97)00385-3.

Liu, D., Pan, B.Z., Zhou, Y.F., et al., 2017. Fluid identification method based on high-resolution array induction logging using GA-SVM. Prog. Geophys. 32 (5), 2051–2056. https://doi.org/10.6038/pg20170526 (in Chinese).

Newgord, C., Posenato Garcia, A., Heidari, Z., 2020. Joint interpretation of electrical resistivity and T2 NMR measurements to estimate wettability and water saturation. SPE Reservoir Eval. Eng. 23 (2), 772–782. https://doi.org/10.2118/200499-pa.

Pickett, G.R., 1966. A review of current techniques for determination of water saturation from logs. J. Petrol. Technol. 18 (11), 1425–1433. https://doi.org/10.2118/1446-pa.

Poupon, A., Leveaux, J., 1971. Evaluation of water saturation in shaly formations. In: SPWLA 12th Annual Logging Symposium. Dallas, Texas.

Poupon, A., Loy, M.E., Tixier, M.P., 1954. A contribution to electrical log interpretation in shaly sands. J. Petrol. Technol. 6 (6), 27–34. https://doi.org/10.2118/311-g.

Prammer, M.G., Mardon, D., Coates, G.R., et al., 1995. Lithology-independent gas detection by gradient-NMR logging. In: SPE Annual Technical Conference and Exhibition. Dallas, Texas.

Qin, Z., Wang, G., Zhang, Y., et al., 2023. A novel evaluation scheme of resistivity anisotropy in near-tight sandstones using conventional geophysical logs: a case study of the Triassic Chang 8 oil layer, Zhenjing area, Ordos Basin. J. Appl. Geophys. 213, 105017. https://doi.org/10.1016/j.jappgeo.2023.105017.

Shah, J.M., Dahlan, N.A.M., Kamarulzaman, M.N., et al., 2019. The revelation of minor reservoir opportunity: realizing low resistivity contrast reservoir play type in Baram Delta Basin East Malaysia, Thru REM log enhancement and comprehensive water salinity analysis. In: SPE Middle East Oil and Gas Show and Conference. https://doi.org/10.2118/194917-ms. Manama, Bahrain.

Simandoux, P., 1963. Dielectric measurements in porous media and application to shaly formation: Revue del'Institut Francais du Petrole. Supplementary Issue, pp. 193–215.

Simpson, G.A., Menke, J.Y., 2010. Identifying low contrast-low resistivity pay zones with pulsed neutron capture logs in shaly sand Miocene Formations of South Louisiana. In: SPWLA 51st Annual Logging Symposium. Perth, Australia.

Shi, W., Wang, X., Shi, Y., et al., 2019. Application of dipole array acoustic logging in the evaluation of shale gas reservoirs. Energies 12 (20), 3882. https://doi.org/10.3390/en12203882.

Tathed, P., Han, Y., Misra, S., 2018. Hydrocarbon saturation in Bakken Petroleum System based on joint inversion of resistivity and dielectric dispersion logs. Fuel 233, 45–55. https://doi.org/10.1016/j.fuel.2018.06.019.

Toumelin, E., Torres-Verdin, C., Sun, B., et al., 2004. A numerical assessment of modern borehole NMR interpretation techniques. In: SPWLA SPE Annual Technical Conference and Exhibition. Houston, Texas. https://doi.org/10.2118/90539-ms.

Waxman, M.H., Smits, L.J.M., 1968. Electrical conductivities in oil-bearing shaly sands. Soc. Petrol. Eng. J. 8 (2), 107–122. https://doi.org/10.2118/1863-a.

Waxman, M.H., Thomas, E.C., 1974. Electrical conductivities in shaly sands-i. the relation between hydrocarbon saturation and resistivity index; ii. the temperature coefficient of electrical conductivity. J. Petrol. Technol. 26 (2), 213–225. https://doi.org/10.2118/4094-pa.

Zhu, L., Ma, Y., Cai, J., et al., 2022. Key factors of marine shale conductivity in southern China—Part II: the influence of pore system and the development direction of shale gas saturation models. J. Petrol. Sci. Eng. 209, 109516. https://doi.org/10.1016/j.petrol.2021.109516.